Supporting information

Benchmarking operando neutron diffraction for high-power Li-ion battery

Dat Le Thanh[a,b,c], Claire Villevieille[d], Romain Berthelot[b,e], Emmanuelle Suard[a]

[a] Institut Laue-Langevin (ILL), 38042, Grenoble, France

[b] ICGM, Université de Montpellier, CNRS, ENSCM, 34095, Montpellier, France

[c] Alistore-European Research Institute, CNRS FR 3104, 80039, Amiens, France

[d] Univ. Grenoble Alpes, Univ. Savoie Mont Blanc, CNRS, Grenoble INP, LEPMI, Grenoble, 38000 France

[e] Réseau sur le Stockage Électrochimique de l'Énergie (RS2E), CNRS, 80039, Amiens, France

Note S1.

Since the first *custom-made* cells introduced in 1998 [1,2], several cell designs have been developed and can be divided into three main categories: coin-type**,** pouch-type, and cylindrical roll-over cells [3–23].

In coin-type cells, loose powder or self-standing composite are housed in a compartment exposed to the neutron beam. Casings made from PEEK, aluminium, or titanium have been tested, but can introduce background features or Bragg reflections that overlap with signals from the electroactive material [7–14]. To address this issue, the coin-type cell developed by Bianchini *et al.* used a neutron-transparent $Ti_{2.1}Zr$ alloy for the cell body, resulting in the absence of Bragg peaks and a low background [15,24]. However, the remaining trade-off is that the relatively thick electrode required for adequate signal-to-noise ratio diffraction and suitable temporal resolution, induces polarization, which in turn limits the achievable cycling rates.

Pouch-type cells recently gained interest due to large material quantity while having flexibility in component choice with stacked electrodes and separators enclosed in a heat-sealed, propylene-coated aluminium pouch. While this design provides better electrochemical performance and supports higher cycling rates, it also suffers from significant background noise due to polymer coating and anisotropic absorption due to the non-radial geometry of the cell [3–6].

Finally, the cylindrical roll-over configuration represents another key advance. These cells are assembled by rolling the electrode, separator, and lithium foil into a cylinder, filling with electrolyte, and sealing the assembly. All reported *operando* cylindrical cells employed deuterated electrolytes to minimize background scattering but differed in optimization strategies such as electrode loading, casing materials, separator type, and connection design. Sharma *et al.* first demonstrated a roll-over cell with ~0.5 g of electroactive material (MoS_2, $Li_4Ti_5O_{12}$, $LiFePO_4$) on Cu/Al collectors and a vanadium casing, achieving *operando* data suitable for phase fraction and lattice parameters refinement [16–19]. Edström group later adapted this concept using quartz or aluminum casings with Swagelok-type joints, and higher active material loadings (1–2 g). Despite long acquisition times (up to 15 h per pattern), their half-cell studies of $LiFePO_4$ and $Li_{0.18}Sr_{0.66}Ti_{0.5}Nb_{0.5}O_3$ allowed structural refinements of unit cell parameters and atomic coordinates for *in situ* NPD patterns at specific states of charge

[20,25]. Villevieille's group further advanced the cell design [21–23,26]. Their first cylindrical cell was a modified industrial prototype that could achieve faster cycling rates up to 15C in stroboscopic *operando* mode, but these studies required industrial collaboration [21,22]. This design was further modified to improve the neutron diffraction data quality by replacing the Fe casing with aluminum and optimized separators using alumina/PET composites, which resulted in reduced parasitic scattering and fast cycling up to C/7 rate. With ~4 g of electroactive material, this configuration achieved 40-minutes data acquisitions in a low intensity sources, suitable for Rietveld refinement and quantification of Li consumption during extended cycling [26]. In the latest version, they developed a cell that could be used assembled in laboratory and looking like an industrial cylindrical cell. They performed a proof-of-concept experiment with $LiNi_{0.6}Co_{0.2}Mn_{0.2}O_2$ (NMC622) half-cell *vs.* Li. The home-made cylindrical cell delivers good electrochemical performance at C/20 with high-quality NPD data, allowing the refinement of Li occupancy and oxygen positions after background correction [23].

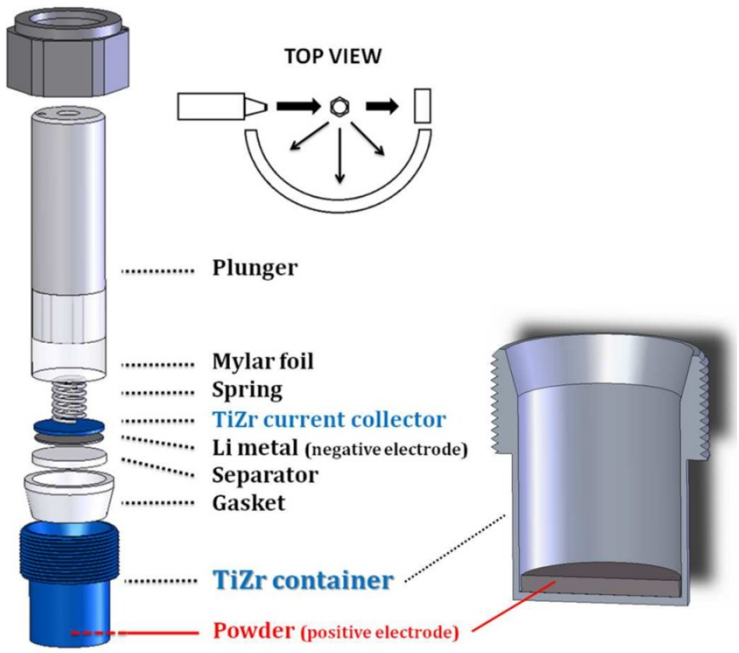

Figure S1. Coin-type *in situ* cell for neutron powder diffraction [15]

X-ray diffractogram and crystallographic structure of monoclinic $FeNb_{11}O_{29}$

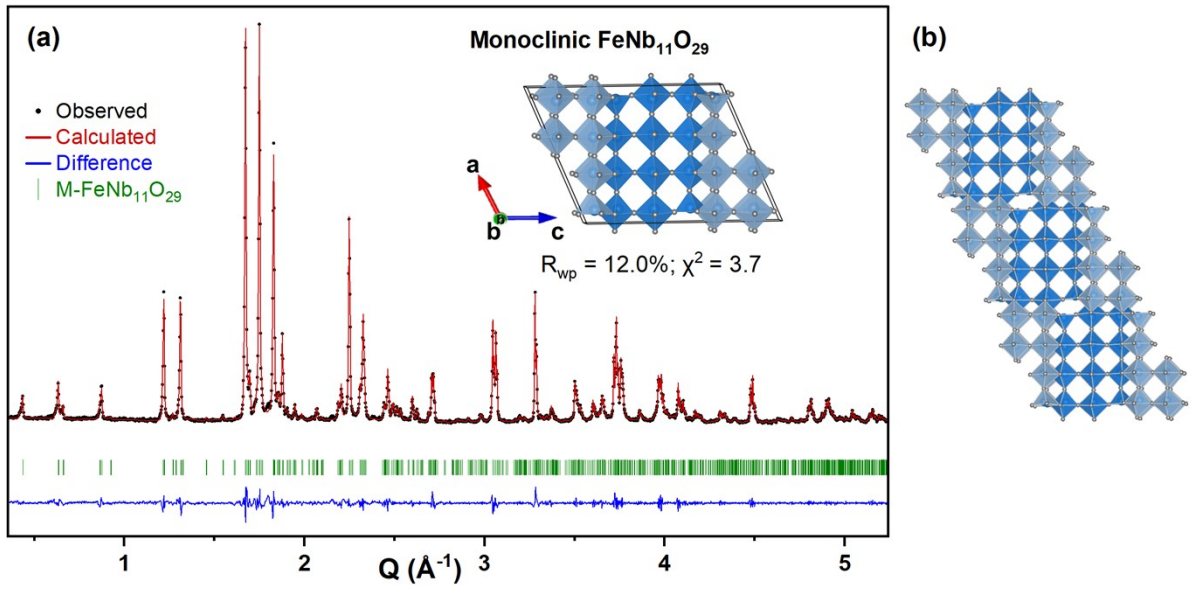

Figure S2. (a) Le Bail-refined XRD pattern of pristine monoclinic $FeNb_{11}O_{29}$ (collected on Panalytical X'pert diffractometer, Cu $K\alpha_{1,2}$) and its crystal structure, and (b) its *trans* connectivity between the blocks

The monoclinic structure of $FeNb_{11}O_{29}$, belonging to Wadsley–Roth family, is constructed from blocks of 4×3 $Nb(Fe)O_6$ octahedra. Within each block, the octahedra are corner-connected, while adjacent blocks are linked by edge-sharing, generating crystallographic shear planes that accommodate oxygen deficiencies. In the monoclinic phase, these blocks are connected at the same level through trans corner-sharing (Figure S4b).

Note S1. Assembling procedure of cylindrical cell

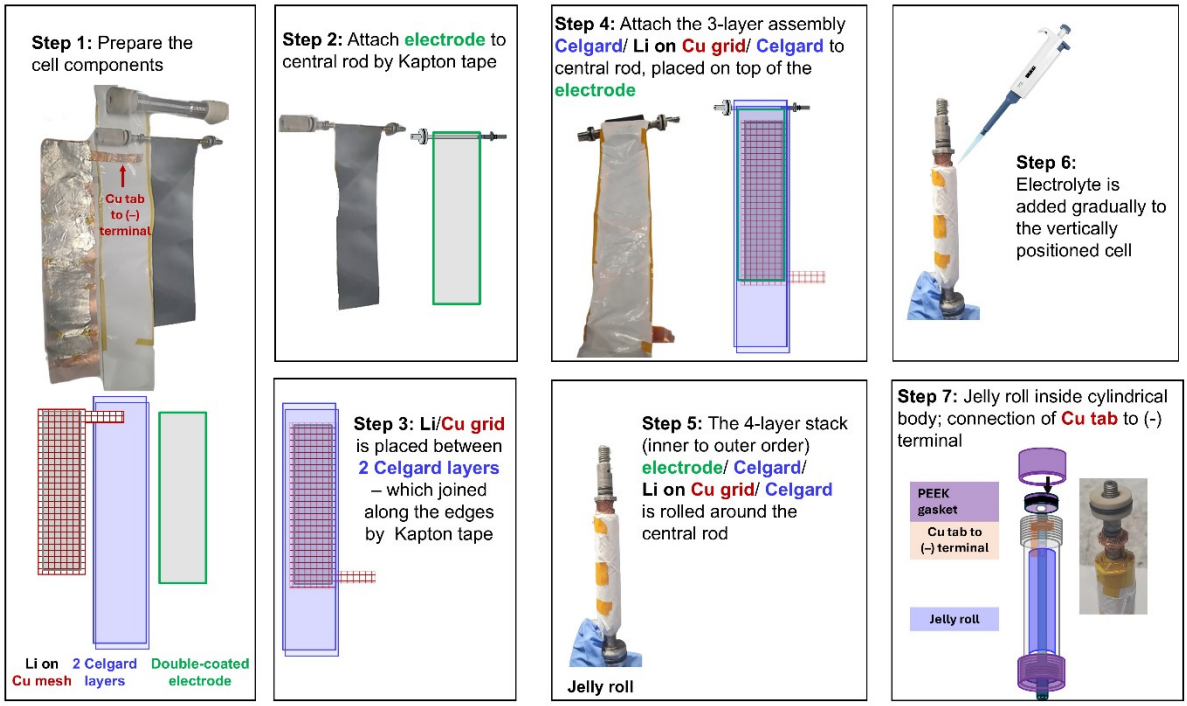

Figure S3. Schematics showing the different step for the assembling procedure of cylindrical cell.

The assembly procedure is shown in Figure S3. The double-coated electrode of active material (5.5 × 20 cm) was paired with Li foil supported on a copper grid of the same size, which served as the counter/reference electrode and is connected to the negative terminal by a Cu tab. The Cu grid edges were covered with Kapton tape to prevent puncture to the separator. Two Celgard strips (6 × 30 cm) were joined along their long edges with Kapton tape to ensure electrical insulation, and the Cu–Li assembly was placed between them. All components were dried overnight at 60 °C (except Li) and assembled in an Ar-filled glovebox. The electrode was attached to the central $Ti_{2.08}Zr$ rod with Kapton tape, and the 4-layer stack (electrode/Celgard/Li on Cu/Celgard) was carefully rolled around it, ensuring tightness and proper alignment. After verifying electrical insulation and sealing the jelly roll, the negative tab was connected to the terminal.

A total of 2 mL of conventional organic electrolyte (1 M $LiPF_6$ in EC:DMC=3:7 by volume) was gradually and uniformly added to the jelly roll. First, the cell was held vertically, and approximately 0.2 mL of electrolyte was evenly distributed along the top edges, ensuring uniform wetting of the layers and different positions within the roll. After each addition, a 2-minute waiting period was maintained to allow for electrolyte distribution due to gravity. Once 1 mL of electrolyte had been added, the cell was kept in this vertical position for an additional

10 minutes. The cell was then inverted (bottom to top), and the process was repeated until a total of approximately 2 mL of electrolyte had been added with thorough and uniform wetting of the jelly roll."

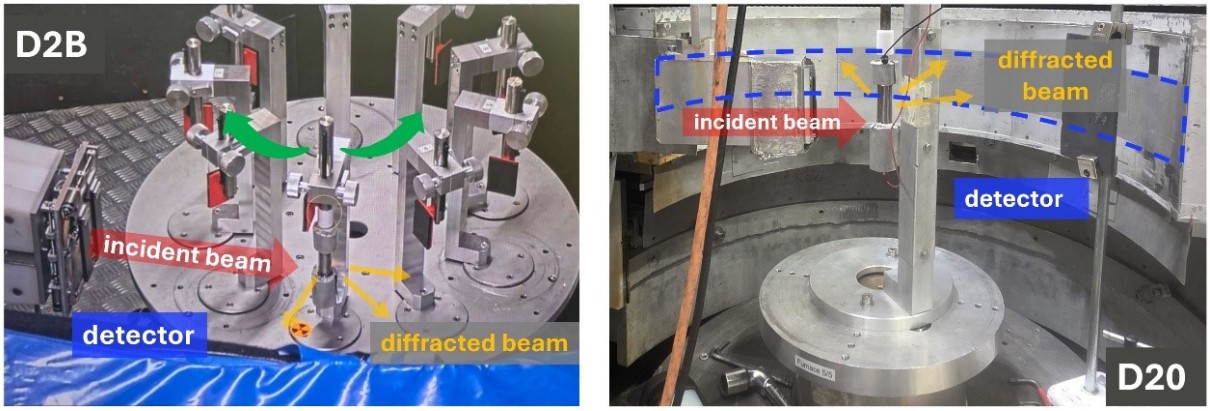

Figure S4. Cylindrical cell mounted at D2B and D20 diffractometers at the ILL

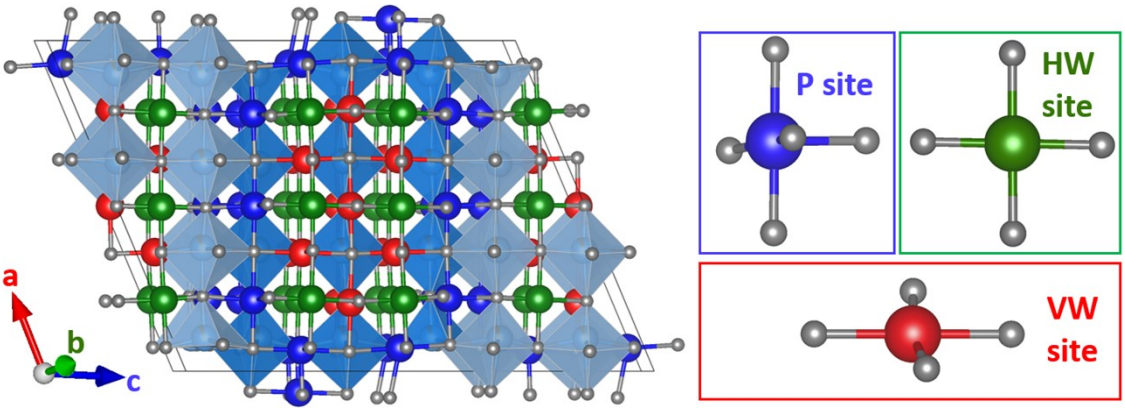

Figure S5. Monoclinic $FeNb_{11}O_{29}$ structure with three types of lithium sites: pocket sites (P, blue), horizontal window (HW, green) and vertical window (VW, red) sites.

Monoclinic $FeNb_{11}O_{29}$ exhibits three types of lithium sites (Figure S7):

- 5 pocket sites (P) at edge-sharing positions, characterized by five-fold coordination.
- Window sites, which are four-fold coordinated, can be further divided into:
  - 3 horizontal window (HW) sites, coordinated by four oxygen atoms in the block plane (ac-plane).
  - 4 vertical window (VW) sites, coordinated by four oxygen atoms in the planes perpendicular to the block.

Table S1. Three types of lithium sites in monoclinic $FeNb_{11}O_{29}$ with their Wykoff position and atomic coordinates

Li site	Wyckoff position	x/a	y/b	z/c	Site
Li1	4i	0.0640	0	0.2646	P
Li2	4i	0.0700	0	0.4773	P
Li3	4i	0.2150	0	0.2074	P
Li4	4i	0.2210	0	0.6261	P
Li5	4i	1/2	0	0.2941	P
Li6	2a	1/2	1/2	0	VW
Li7	4i	0.2075	0	0.4128	VW
Li8	4i	0.3600	1/2	0.0541	VW
Li9	4i	0.3585	0	0.3556	VW
Li10	4i	0.4975	0	0.0947	HW
Li11	4i	0.2180	0	0.8188	HW
Li12	4i	0.2160	0	0.0162	HW

This unit cell contains $(4 \times 5) + (4 \times 3 + 2) + (4 \times 3) = 46$ Li sites. With two formula units (f.u.) of $FeNb_{11}O_{29}$ per unit cell, this corresponds to $46 / 2 = 23$ Li sites per f.u.

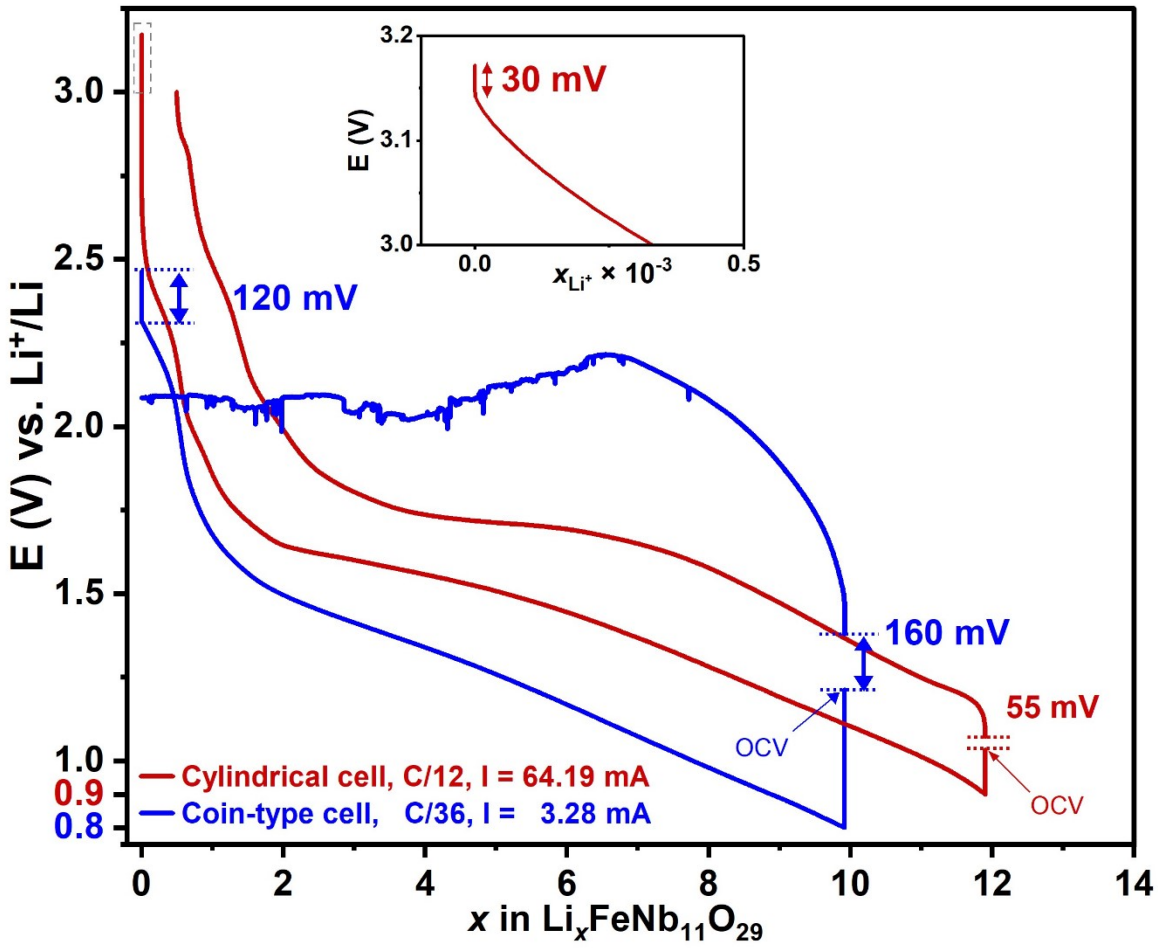

Figure S6. Galvanostatic cycling curves of cylindrical and coin-type operando cells. The voltage step ΔE at the start of discharge and charge is used to estimate the internal resistance (R = ΔE/I). The cylindrical cell shows a much lower internal resistance (< 1 Ω) than the coin-type cell (~30–50 Ω).

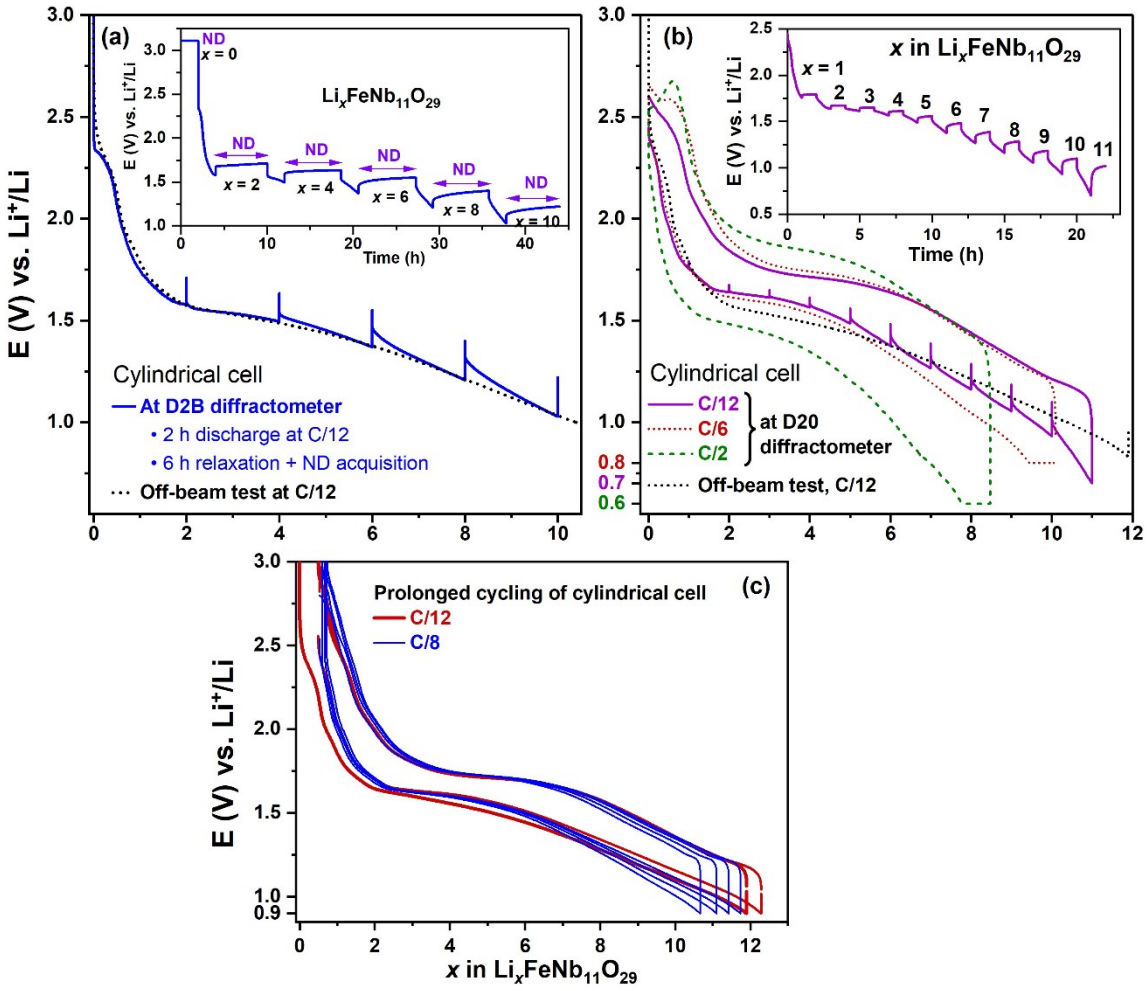

Figure S7. Charge-discharge profiles of $FeNb_{11}O_{29}$/Li half-cell in cylindrical configuration during *in situ/operando* experiments at (a) D2B and (b) D20 diffractometers, and (c) prolonged cycling test.

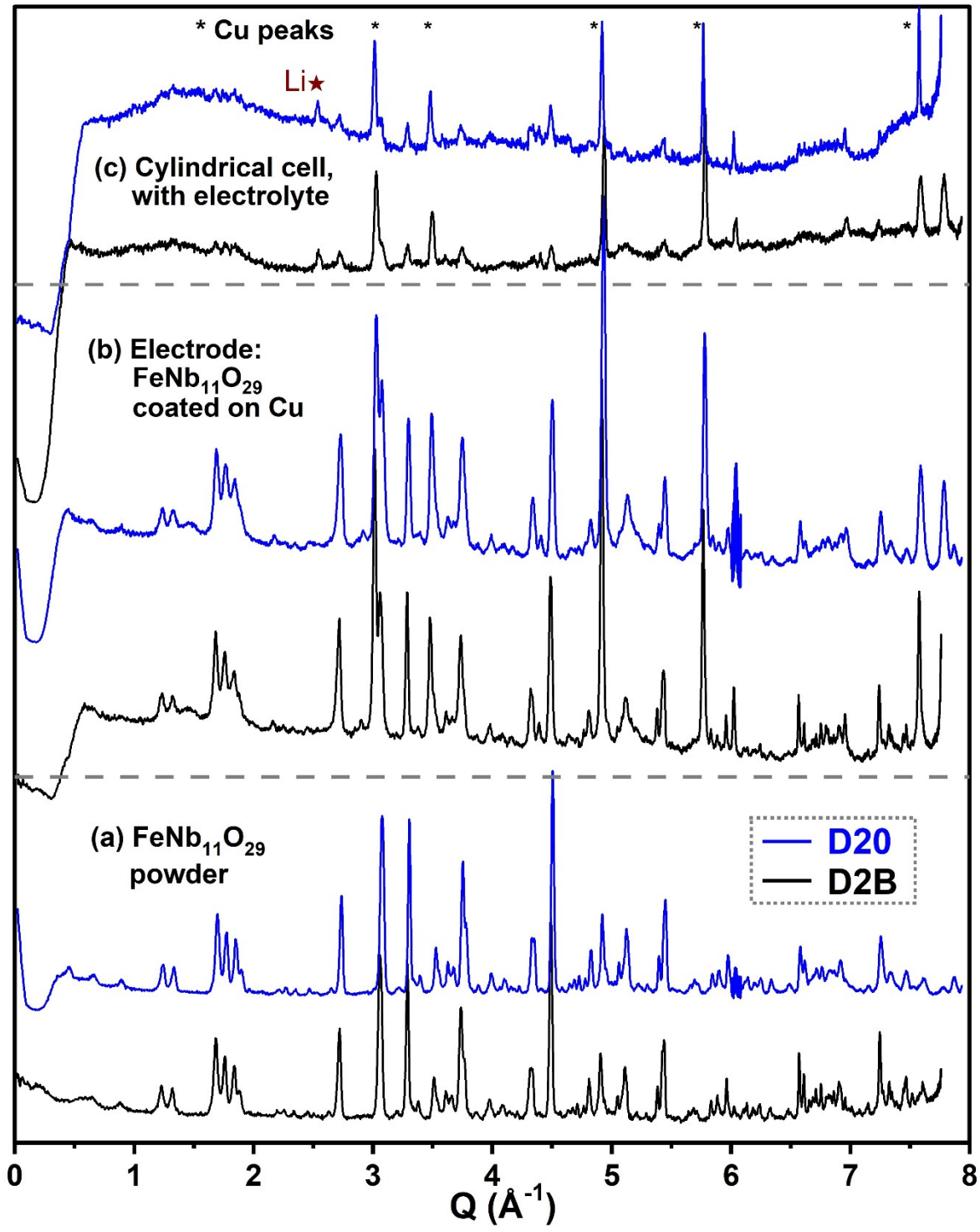

Figure S8. Comparison of ND patterns obtained at D2B and D20 diffractometers for (a) $FeNb_{11}O_{29}$ powder, (b) electrode of $FeNb_{11}O_{29}$ coated on Cu foil, and (c) cylindrical cell filled with electrolyte. Data in Q = 5.9–6.1 $Å^{-1}$ region were fluctuated due to faulty detectors.

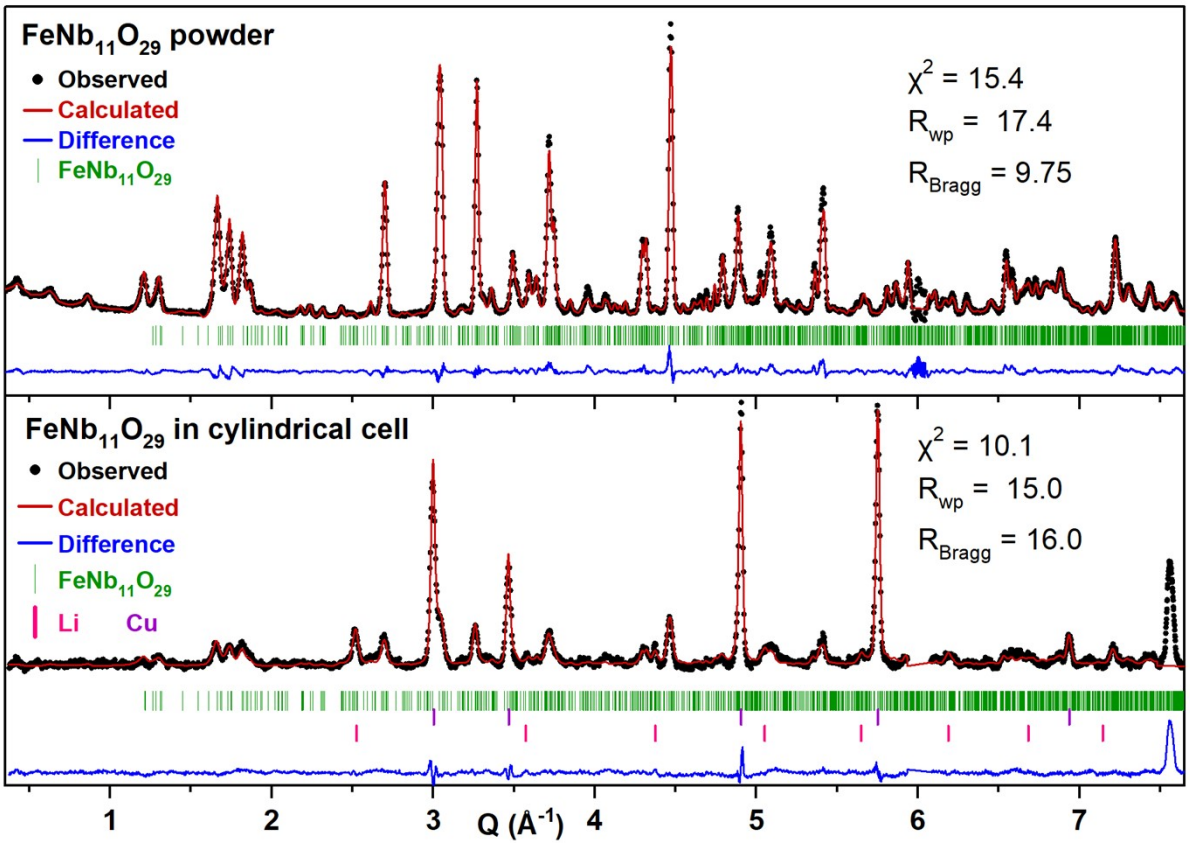

Figure S9. Rietveld-refined NPD patterns obtained at D20 beamline of $FeNb_{11}O_{29}$ powder and cylindrical cell after background subtraction, fitted with $FeNb_{11}O_{29}$ (green), Cu (purple), and Li (pink). Data in Q = 5.9–6.1 $Å^{-1}$ region were excluded due to faulty detectors.

Table S2. Rietveld refinement results of ND patterns of $FeNb_{11}O_{29}$ phase in cylindrical cell

Neutron diffraction		**$FeNb_{11}O_{29}$**		***A*2/*m***	**Z = 2**	
	a (Å) 15.623(2)	*b* (Å) 3.8494(3)		*c* (Å) 20.694(2)	*β* 113.025(11)°	α = γ = 90°
Atom	Wyckoff position	Atomic coordinates *x*/*a*	*y*/*b*	*z*/*c*	Occ.	B_{iso} (Å^2)
Nb1/Fe1	4*i*	0.0942(2)	0.0	0.0663(2)	0.92/0.08	3.857
Nb2/Fe2	4*i*	0.0846(3)	0.0	0.6912(3)	0.92/0.08	3.718
Nb3/Fe3	4*i*	0.0945(3)	0.0	0.8826(3)	0.92/0.08	3.825
Nb4/Fe4	4*i*	0.3783(2)	0.0	0.1517(2)	0.92/0.08	3.185
Nb5/Fe5	4*i*	0.3725(3)	0.0	0.7805(3)	0.92/0.08	3.292
Nb6/Fe6	4*i*	0.3708(3)	0.0	0.9568(3)	0.92/0.08	3.142
O1	2*d*	0.5000	0.0	0.0000	0.5	6.622
O2	4*i*	0.0649	0.0	0.1665	1.0	4.458
O3	4*i*	0.0884	0.0	0.3667	1.0	4.849
O4	4*i*	0.0788	0.0	0.5873	1.0	4.624
O5	4*i*	0.0763	0.0	0.7773	1.0	6.014
O6	4*i*	0.0809	0.0	0.9855	1.0	6.209
O7	4*i*	0.2263	0.0	0.1075	1.0	5.653
O8	4*i*	0.2259	0.0	0.7267	1.0	5.755
O9	4*i*	0.2186	0.0	0.9169	1.0	4.593
O10	4*i*	0.3653	0.0	0.0516	1.0	4.065
O11	4*i*	0.3510	0.0	0.2479	1.0	6.513
O12	4*i*	0.3510	0.0	0.4514	1.0	5.176
O13	4*i*	0.3581	0.0	0.6641	1.0	4.191
O14	4*i*	0.3555	0.0	0.8610	1.0	5.110
O15	4*i*	0.5017	0.0	0.1901	1.0	4.414
R_{wp} = 12.3%, Bragg R-factor = 19.1%, RF-factor = 14.6%						

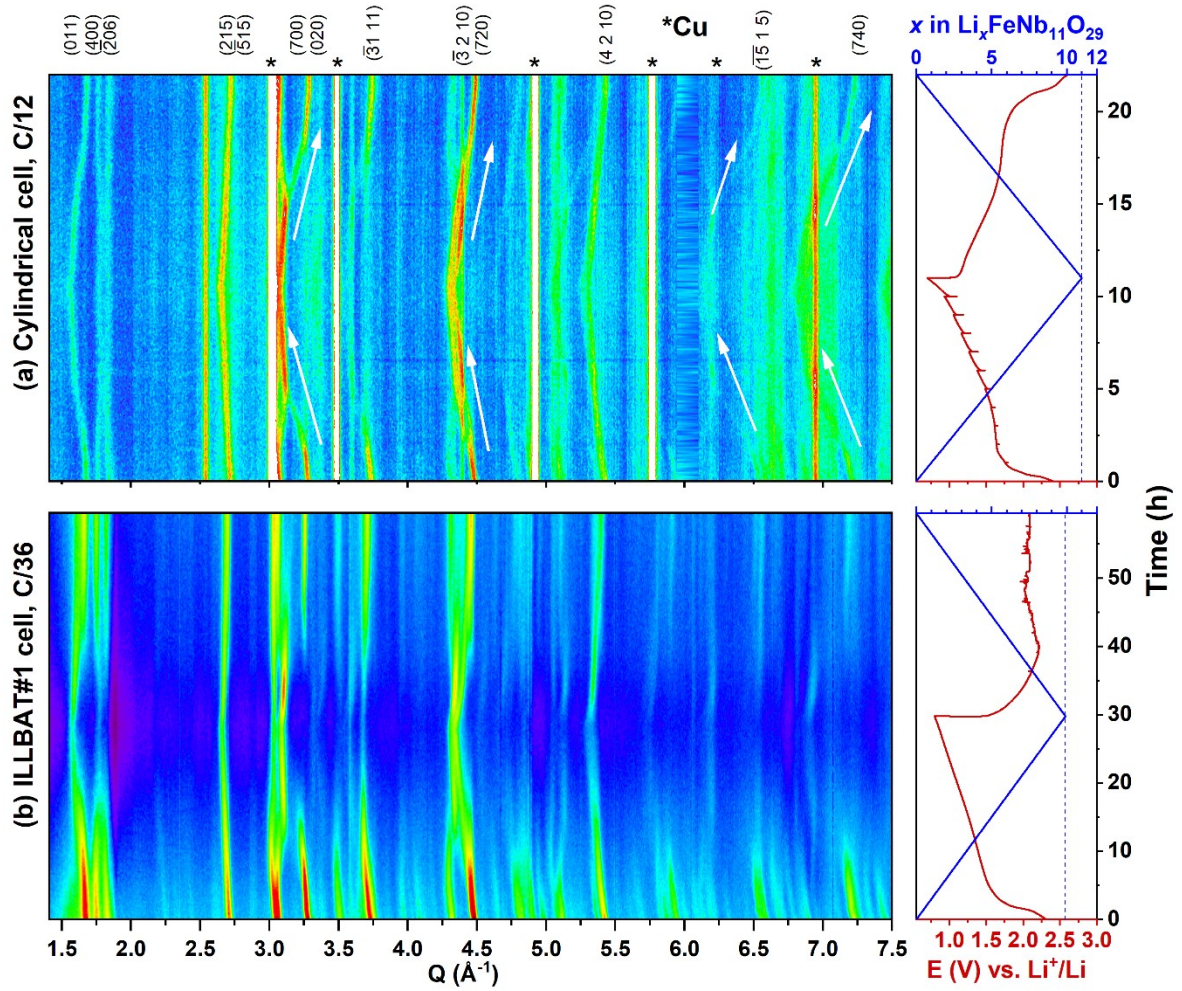

Figure S10. *Operando* NPD contour plots of $FeNb_{11}O_{29}$/Li half-cells collected at D20 diffractometer using (a) a cylindrical cell (C/12) and (b) the coin-type cell (C/36). Peak shifts are observed in the cylindrical cell, while the coin-type cell shows weaker or discontinuous changes.

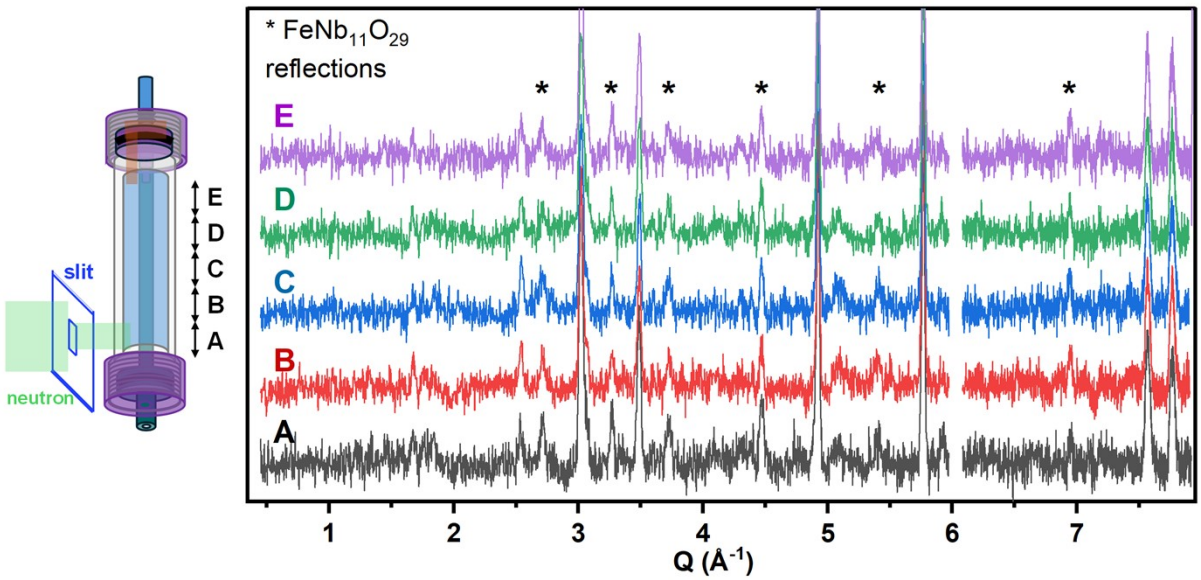

Figure S11. Vertical NPD scans obtained on D20 diffractometer at different electrode positions (A–E) show consistent $FeNb_{11}O_{29}$ reflections (asterisks), confirming uniform electrochemical reactions throughout the cell.

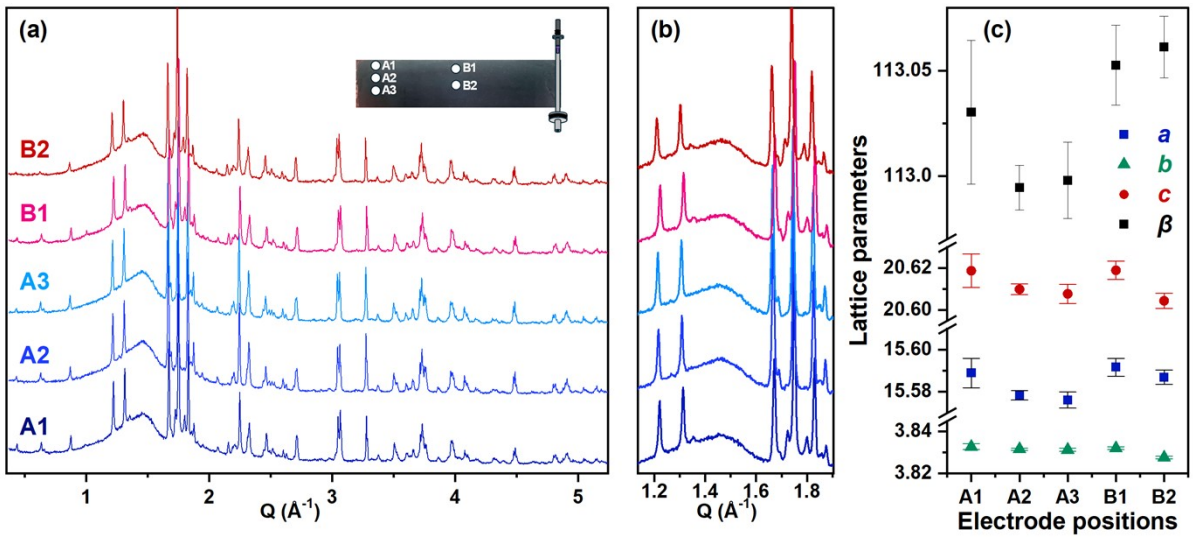

Figure S12. Post-mortem laboratory XRD from different electrode positions shows nearly identical peak positions and minor lattice variations, confirming structural homogeneity.

Table S3. Refined lattice parameters of $FeNb_{11}O_{29}$ electrodes at different positions

Samples	**a (Å)**	**b (Å)**	**c (Å)**	**β (°)**	χ^2	R_{wp}
A1	15.589(2)	3.8627(5)	20.619(3)	113.030(11)	18.0	6.37
A2	15.5783(8)	3.8315(2)	20.6099(9)	112.9944(13)	7.49	6.13
A3	15.5761(13)	3.8313(3)	20.6078(15)	112.9978(6)	11.2	7.43
B1	15.5917(14)	3.8320(2)	20.6189(15)	113.053(6)	9.70	6.94
B2	15.5870(11)	3.8276(2)	20.6044(12)	113.061(5)	7.01	6.00

References

[1] Ö. Bergstöm, A.M. Andersson, K. Edström, T. Gustafsson, A neutron diffraction cell for studying lithium-insertion processes in electrode materials, J Appl Crystallogr 31 (1998) 823–825. https://doi.org/10.1107/S002188989800538X.

[2] H. Berg, H. Rundlöv, J.O. Thomas, The $LiMn_2O_4$ to λ-MnO2 phase transition studied by in situ neutron diffraction, Solid State Ionics 144 (2001) 65–69. https://doi.org/10.1016/S0167-2738(01)00894-3.

[3] W.K. Pang, V.K. Peterson, A custom battery for operando neutron powder diffraction studies of electrode structure, J Appl Cryst 48 (2015) 280–290. https://doi.org/10.1107/S1600576715000679.

[4] W.K. Pang, N. Sharma, V.K. Peterson, J.-J. Shiu, S. Wu, In-situ neutron diffraction study of the simultaneous structural evolution of a $LiNi_{0.5}Mn_{1.5}O_4$ cathode and a $Li_4Ti_5O_{0.12}$ anode in a $LiNi_{0.5}Mn_{1.5}O_4||Li_4Ti_5O_{0.12}$ full cell, Journal of Power Sources 246 (2014) 464–472. https://doi.org/10.1016/j.jpowsour.2013.07.114.

[5] W.K. Pang, S. Kalluri, V.K. Peterson, S.X. Dou, Z. Guo, Electrochemistry and structure of the cobalt-free $Li_{1+x}MO_2$ (M = Li, Ni, Mn, Fe) composite cathode, Phys. Chem. Chem. Phys. 16 (2014) 25377–25385. https://doi.org/10.1039/C4CP02864C.

[6] W.K. Pang, M. Alam, V.K. Peterson, N. Sharma, Structural evolution of electrodes in the NCR and CGR cathode-containing commercial lithium-ion batteries cycled between 3.0 and 4.5 V: An operando neutron powder-diffraction study, J. Mater. Res. 30 (2015) 373–380. https://doi.org/10.1557/jmr.2014.297.

[7] J.J. Biendicho, M. Roberts, C. Offer, D. Noréus, E. Widenkvist, R.I. Smith, G. Svensson, K. Edström, S.T. Norberg, S.G. Eriksson, S. Hull, New in-situ neutron diffraction cell for electrode materials, Journal of Power Sources 248 (2014) 900–904. https://doi.org/10.1016/j.jpowsour.2013.09.141.

[8] X.-L. Wang, K. An, L. Cai, Z. Feng, S.E. Nagler, C. Daniel, K.J. Rhodes, A.D. Stoica, H.D. Skorpenske, C. Liang, W. Zhang, J. Kim, Y. Qi, S.J. Harris, Visualizing the chemistry and structure dynamics in lithium-ion batteries by in-situ neutron diffraction, Sci Rep 2 (2012) 747. https://doi.org/10.1038/srep00747.

[9] B. Vadlamani, K. An, M. Jagannathan, K.S.R. Chandran, An In-Situ Electrochemical Cell for Neutron Diffraction Studies of Phase Transitions in Small Volume Electrodes of Li-Ion Batteries, J. Electrochem. Soc. 161 (2014) A1731–A1741. https://doi.org/10.1149/2.0951410jes.

[10] B. Song, G.M. Veith, J. Park, M. Yoon, P.S. Whitfield, M.J. Kirkham, J. Liu, A. Huq, Metastable $Li_{1+\delta}Mn_2O_4$ ($0 \leq \delta \leq 1$) Spinel Phases Revealed by in Operando Neutron Diffraction and First-Principles Calculations, Chem. Mater. 31 (2019) 124–134. https://doi.org/10.1021/acs.chemmater.8b03199.

[11] P.-H. Chien, X. Wu, B. Song, Z. Yang, C.K. Waters, M.S. Everett, F. Lin, Z. Du, J. Liu, New Insights into Structural Evolution of $LiNiO_2$ Revealed by Operando Neutron Diffraction, Batteries & Supercaps 4 (2021) 1701–1707. https://doi.org/10.1002/batt.202100135.

[12] F. Rosciano, M. Holzapfel, W. Scheifele, P. Novák, A novel electrochemical cell for *in situ* neutron diffraction studies of electrode materials for lithium-ion batteries, J Appl Crystallogr 41 (2008) 690–694. https://doi.org/10.1107/S0021889808018025.

[13] J.-F. Colin, V. Godbole, P. Novák, *In situ* neutron diffraction study of Li insertion in $Li_4Ti_5O_{12}$, Electrochemistry Communications 12 (2010) 804–807. https://doi.org/10.1016/j.elecom.2010.03.038.

[14] V. Godbole, M. Hess, C. Villevieille, H. Kaiser, J.-F. Colin, P. Novak, Circular in situ neutron powder diffraction cell for study of reaction mechanism in electrode materials for

Li-ion batteries, RSC Advances 3 (2013) 757–763. https://doi.org/10.1039/C2RA21526H.
[15] M. Bianchini, J.B. Leriche, J.-L. Laborier, L. Gendrin, E. Suard, L. Croguennec, C. Masquelier, A New Null Matrix Electrochemical Cell for Rietveld Refinements of In-Situ or Operando Neutron Powder Diffraction Data, J. Electrochem. Soc. 160 (2013) A2176–A2183. https://doi.org/10.1149/2.076311jes.
[16] N. Sharma, G. Du, A.J. Studer, Z. Guo, V.K. Peterson, In-situ neutron diffraction study of the MoS_2 anode using a custom-built Li-ion battery, Solid State Ionics 199–200 (2011) 37–43. https://doi.org/10.1016/j.ssi.2011.07.015.
[17] N. Sharma, M.V. Reddy, G. Du, S. Adams, B.V.R. Chowdari, Z. Guo, V.K. Peterson, Time-Dependent in-Situ Neutron Diffraction Investigation of a $Li(Co_{0.16}\ Mn_{1.84}\ )O_4$ Cathode, J. Phys. Chem. C 115 (2011) 21473–21480. https://doi.org/10.1021/jp2026237.
[18] W.R. Brant, S. Schmid, G. Du, H.E.A. Brand, W.K. Pang, V.K. Peterson, Z. Guo, N. Sharma, In Situ Neutron Powder Diffraction Using Custom-made Lithium-ion Batteries, JoVE (2014) 52284. https://doi.org/10.3791/52284.
[19] G. Du, N. Sharma, V.K. Peterson, J.A. Kimpton, D. Jia, Z. Guo, Br-Doped $Li_4Ti_5O_{12}$ and Composite TiO_2 Anodes for Li-ion Batteries: Synchrotron X-Ray and in situ Neutron Diffraction Studies, Adv Funct Materials 21 (2011) 3990–3997. https://doi.org/10.1002/adfm.201100846.
[20] M. Roberts, J.J. Biendicho, S. Hull, P. Beran, T. Gustafsson, G. Svensson, K. Edström, Design of a new lithium ion battery test cell for in-situ neutron diffraction measurements, Journal of Power Sources 226 (2013) 249–255. https://doi.org/10.1016/j.jpowsour.2012.10.085.
[21] L. Boulet-Roblin, P. Borel, D. Sheptyakov, C. Tessier, P. Novák, C. Villevieille, Operando Neutron Powder Diffraction Using Cylindrical Cell Design: The Case of $LiNi_{0.5}Mn_{1.5}O_4$ vs Graphite, J. Phys. Chem. C 120 (2016) 17268–17273. https://doi.org/10.1021/acs.jpcc.6b05777.
[22] D. Sheptyakov, L. Boulet-Roblin, V. Pomjakushin, P. Borel, C. Tessier, C. Villevieille, Stroboscopic neutron diffraction applied to fast time-resolved *operando* studies on Li-ion batteries (d-$LiNi_{0.5}\ Mn_{1.5}\ O_4$ *vs.* graphite), J. Mater. Chem. A 8 (2020) 1288–1297. https://doi.org/10.1039/C9TA11826H.
[23] L. Vitoux, M. Reichardt, S. Sallard, P. Novák, D. Sheptyakov, C. Villevieille, A Cylindrical Cell for Operando Neutron Diffraction of Li-Ion Battery Electrode Materials, Frontiers in Energy Research 6 (2018). https://www.frontiersin.org/articles/10.3389/fenrg.2018.00076 (accessed May 8, 2023).
[24] A.V. Dobromyslov, N.I. Taluts, Structure studies of quenched and tempered Zr-Ti alloys, Fiz. Met. Metalloved.; (USSR) 63:1 (1987). https://www.osti.gov/etdeweb/biblio/5683306 (accessed June 27, 2025).
[25] W.R. Brant, M. Roberts, T. Gustafsson, J.J. Biendicho, S. Hull, H. Ehrenberg, K. Edström, S. Schmid, A large format in operando wound cell for analysing the structural dynamics of lithium insertion materials, Journal of Power Sources 336 (2016) 279–285. https://doi.org/10.1016/j.jpowsour.2016.10.071.
[26] L. Boulet-Roblin, D. Sheptyakov, P. Borel, C. Tessier, P. Novák, C. Villevieille, Crystal structure evolution via operando neutron diffraction during long-term cycling of a customized 5 V full Li-ion cylindrical cell $LiNi_{0.5}Mn_{1.5}O_4$ vs. graphite, J. Mater. Chem. A 5 (2017) 25574–25582. https://doi.org/10.1039/C7TA07917F.